



Letters

Creep of phyllosilicates at the onset of plate tectonics

Elodie Amiguet ^{a,b,c}, Bruno Reynard ^{a,b,c}, Razvan Caracas ^{a,b,c}, Bertrand Van de Moortèle ^{a,b,c}, Nadège Hilairet ^{d,e}, Yanbin Wang ^d

^a Université de Lyon, France

^b CNRS, UMR5276, France

^c Ecole Normale Supérieure de Lyon, Site Monod, 15 parvis René Descartes BP 7000, Lyon, F-69342, France

^d Center for Advanced Radiation Sources, University of Chicago, Chicago, Illinois, USA

^e Now at UMET, UMR 8207 CNRS-Université Lille 1, Villeneuve d'Ascq, France

ARTICLE INFO

Article history:

Received 17 November 2011

Received in revised form

14 June 2012

Accepted 18 June 2012

Editor: L. Stixrude

Available online 20 July 2012

Keywords:

creep

phyllosilicates

plate tectonics

rheology

ABSTRACT

Plate tectonics is the unifying paradigm of geodynamics yet the mechanisms and causes of its initiation remain controversial. Some models suggest that plate tectonics initiates when the strength of lithosphere is lower than 20–200 MPa, below the frictional strength of lithospheric rocks (> 700 MPa). At present-day, major plate boundaries such as the subduction interface, transform faults, and extensional faults at mid-oceanic ridge core complexes indicate a transition from brittle behaviour to stable sliding at depths between 10 and 40 km, in association with water–rock interactions forming phyllosilicates. We explored the rheological behaviour of lizardite, an archetypal phyllosilicate of the serpentine group formed in oceanic and subduction contexts, and its potential influence on weakening of the lithospheric faults and shear zones. High-pressure deformation experiments were carried out on polycrystalline lizardite—the low temperature serpentine variety—using a D-DIA apparatus at a variety of pressure and temperature conditions from 1 to 8 GPa and 150 to 400 °C and for strain rates between 10^{-4} and 10^{-6} s⁻¹. Recovered samples show plastic deformation features and no evidence of brittle failure. Lizardite has a large rheological anisotropy, comparable to that observed in the micas. Mechanical results and first-principles calculations confirmed easy gliding on lizardite basal plane and show that the flow stress of phyllosilicate is in the range of the critical value of 20–200 MPa down to depths of about 200 km. Thus, foliated serpentine or chlorite-bearing rocks are sufficiently weak to account for plate tectonics initiation, aseismic sliding on the subduction interface below the seismogenic zone, and weakening of the oceanic lithosphere along hydrothermally altered fault zones. Serpentinisation easing the deformation of the early crust and shallow mantle reinforces the idea of a close link between the occurrence of plate tectonics and water at the surface of the Earth.

© 2012 Elsevier B.V. All rights reserved.

1. Introduction

Geological and geochemical signatures of rocks from the Early Archean 3.7–3.8 Ga Isua belt (Komiya et al., 1999; Polat et al., 2002) point to an early onset of plate-like tectonics and subduction. The Hf isotope record from Hadean zircons suggests that plate tectonics could have operated as early as 4.4 Ga (Harrison et al., 2005) via foundering and melting of hydrous crust in the mantle (Blichert-Toft and Albarede, 2008). Geodynamical models requires low yield strength materials to generate plate boundaries (Solomatov, 2004; Van Heck and Tackley, 2008). Low yield

* Corresponding author at: Ecole Normale Supérieure de Lyon, Site Monod, 15 parvis René Descartes BP 7000, Lyon, F-69342, France. Tel.: +33 4 72 72 88 24; fax: +33 4 72 72 86 77.

E-mail address: elodie.amiguet@ens-lyon.fr (E. Amiguet).

strength zones may be generated by the formation of weak minerals and rocks at particular sites, or by modifications of rheological properties through damage and grain size reduction during deformation (Bercovici and Ricard, 2012). In a context of strong chemical interaction between the early hydrosphere and lithosphere (Mojzsis et al., 2001), hydrous phyllosilicates like serpentine and chlorite form and may provide mechanically weak nucleation sites for subduction and plate tectonics (Hilairet et al., 2007).

Serpentine minerals are common in deep portion of faults (Reinen et al., 1991) and ultramafic rocks in the oceanic lithosphere at slow-spreading ridges (Escartin et al., 1997a) and play a major role on the dynamic of subduction zones. Structures of serpentine variety minerals depend on temperature conditions. While antigorite is the high-temperature serpentine mineral, lizardite is stable for temperatures below 300 °C (Evans, 2004). Previous deformation experiments on serpentine minerals at

moderate pressure (< 1 GPa) and room temperature showed a low coefficient of friction ($\mu=0.15\text{--}0.35$) for lizardite serpentinites (Reinen et al., 1994) and a coefficient of friction comparable with other crustal rocks for antigorite serpentinites (Reinen et al., 1991). At large loading velocity, serpentines display velocity weakening, but at low velocities more representative of plate motion rates, they display velocity-strengthening behaviour resulting in stable sliding on natural faults (Moore et al., 1997; Reinen et al., 1991). Deformation experiments using Griggs and Paterson apparatuses for pressure up to 1 GPa and temperature up to 700 °C showed a brittle-ductile transition at 0.2 to 0.5 GPa for lizardite- and antigorite-serpentinites respectively (Byerlee, 1978; Escartin et al., 1997b; Moore et al., 1997; Murrell and Ismail, 1976; Raleigh and Paterson, 1965).

In spite of the potential predominance of ductile regime at high pressure, few studies focused on the rheological behaviour of serpentine for pressures above 1 GPa. Experiments on the rheological behaviour of antigorite for pressures up to 4 GPa using D-DIA apparatus and *in situ* measurements (Hilairet et al., 2007) suggested plastic behaviour and demonstrated flow strength an order of magnitude lower than dry lithospheric rocks (Mei et al., 2010). The yield strength of antigorite is compatible with the yield strength below the threshold of 20–200 MPa at geological strain rates. However, extrapolations from laboratory strain rates ($10^{-4}\text{--}10^{-6}$ s $^{-1}$) to tectonic strain rate (as low as 10^{-15} s $^{-1}$) have large uncertainties because they are based on empirical rheological laws (Chernak and Hirth, 2010; Hilairet et al., 2007).

Finally the structural differences in serpentine variety may influence the deformation mechanisms and rheological behaviour (Hirauchi et al., 2010). The present study focuses on high pressure rheological behaviour of lizardite, the low temperature and the simplest flat-layer structured serpentine variety. Lizardite is found in the first metamorphic transformations associated with active oceanic subduction zones (Evans, 2004; Maekawa et al., 1993). It is a common serpentine mineral along mid-ocean ridges (Mével, 2003) either where extensional weak faults exhume mantle peridotites at the axis of magma-poor regions (Escartin, 2003) or along transform faults (Reinen et al., 1994).

2. Material and methods

2.1. Samples

The starting material is a natural lizardite – serpentinite from Monte Fico, Elba Island, Italy. It is a euhedral lizardite-1T polytype with structural formula $\text{Mg}_{2.74}\text{Fe}_{0.16}\text{Al}_{0.09}\text{Si}_{1.93}\text{Al}_{0.07}\text{O}_5(\text{OH})_4$ (Mellini and Viti, 1994). The sample was ground and sieved to obtain two powders, one with grain sizes below 10 μm and one

with grain sizes ranging from 50 to 100 μm (Fig. 1). These two powders were cold-pressed manually into 1.2 mm length and 1.2 mm high cylinders and placed into h-BN sleeves. Gold foils, (5 μm thick) were placed at each end of the sample to serve as strain markers (Fig. 2a). Specimens were deformed in between two densified alumina pistons. Along the compression column we used two crushable alumina pistons in order to accommodate cold compression deformation. This assembly was loaded into a graphite sleeve, used as a resistive heater and then placed into a $7 \times 7 \times 6$ cubic pressure medium composed of boron epoxy (5:1 by weight).

2.2. Deformation experiments

High pressure deformation experiments with *in-situ* stress and strain measurements were carried out using a D-DIA apparatus in a 250-T Large Volume Press (LVP) coupled with monochromatic ($\lambda=0.24796$ Å and $\lambda=0.27552$ Å) synchrotron light source at the GeoSoilEnviroCARS (Wang et al., 2003, 2009) (Sector 13), Advanced Photon Source (APS), Argonne National Laboratory. Fourteen deformation cycles were performed on four specimens at pressures (P) and temperatures (T) ranging from 1 to 8 GPa and 150 to 400 °C, at strain rates ($\dot{\epsilon}$) between 10^{-4} and 10^{-6} s $^{-1}$.

In all experiments, specimens were first cold compressed to the desired confining pressure using the main hydraulic ram. Temperature was then increased and maintained constant over 30 min to 1 h. The temperature was generated with an AC current transmitted by the vertical tungsten carbide anvils and applied to the graphite furnace. Temperature was measured with one or two W3%Re–W26%Re thermocouples which junctions made by mechanical contact with the outer wall of the furnace. During the temperature raise of each experiment, electrical power delivered to the graphite furnace was calibrated against temperature. These calibrations were used to control the temperature by monitoring the power after thermocouple failure which always occurred at the beginning of the deformation cycle at high pressure and temperature. The uncertainty on temperature was $\pm 10\%$. This uncertainty is not critical for the present results because temperature has little effect on the plasticity of lizardite.

Sample strain was generated using the differential rams independently from the confining pressure. Both inner (vertical) rams of the D-DIA were advanced towards each other at a constant rate to deform the cell assembly by axial compression until specimen steady-state deformation was reached in the sample at constant temperature and confining pressure. Differential rams were then reversed to elongate the sample back to a length close to the original one. Once such a deformation cycle is performed, the set of processing parameters (e.g. temperature, differential ram speed) was changed and a new cycle started. Each

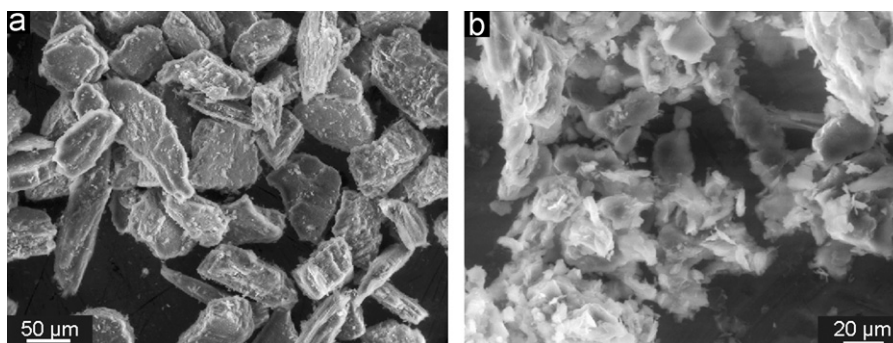


Fig. 1. Environmental Scanning Electron Microscopy images of the starting lizardite powders. (a) Coarse-grained powder with average grain size between 50 and 100 μm . (b) Fine-grained powder with grain size below 10 μm .

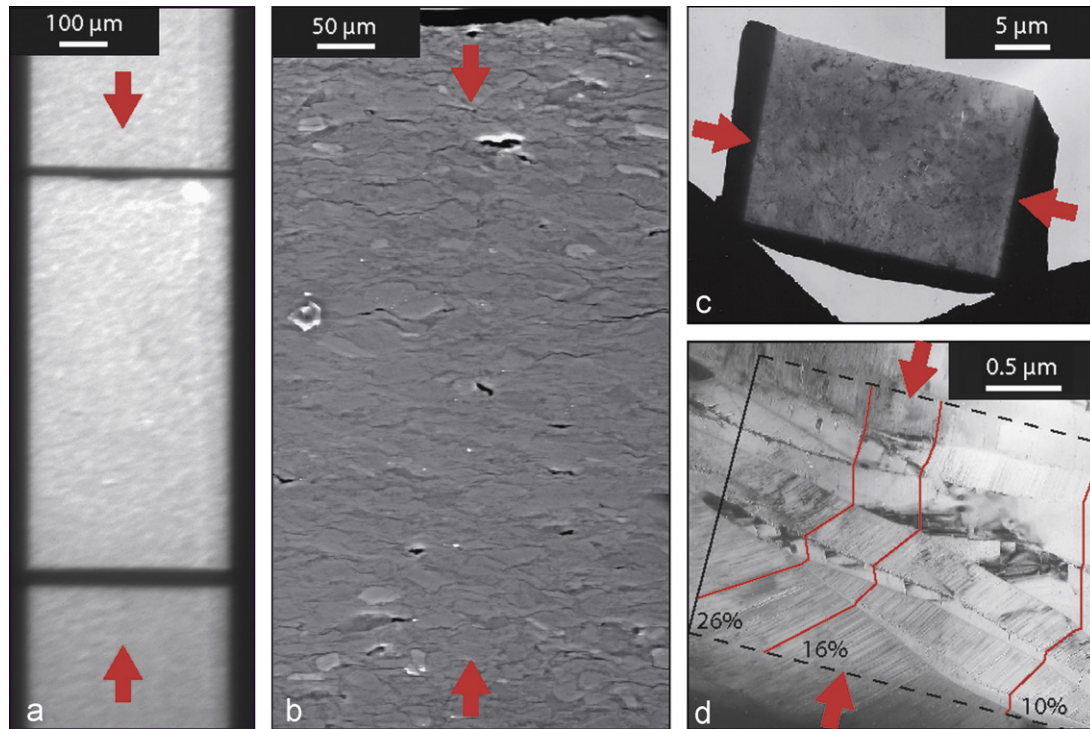


Fig. 2. Images of the deformed sample. (a) X-ray radiography of the lizardite sample in the press during deformation at $P=8$ GPa and $T=250$ °C; the sample is lined with two gold foils appearing as black horizontal lines. (b) ESEM image of fine grained sample deformed at 8 GPa showing homogeneous deformation marked by alignment of lizardite (001) flakes perpendicular to compression. (c) FIB thin section and (d) TEM image showing lizardite deformation by glide along (001) and kinking. Maximum apparent deformation is calculated by unkinking the traces of (001) planes (red broken lines) parallel to compression axis (thick arrows).

sample experienced deformation at only one confining pressure. Low temperature deformation cycles were performed first in all experiments. At the end of the runs, the furnace power was turned off to quench the samples. Pressure was then decreased in 6, 2.5 and 1 h from 40, 20 and 8 t to room pressure respectively, in order to preserve samples from additional cold deformation.

2.3. *In situ* strain measurements

The sample length was defined by the distance between the gold foils seen as black lines of X-Ray absorption at the top and bottom of the sample (Fig. 2a). These strain markers allowed *in-situ* sample length measurements as a function of time during deformation in axial compression. Sample length was measured for each 1 pixel column of the whole width of the sample (300 pixels) and then averaged. A reference sample length was defined at zero differential stress state, for each deformation cycle in axial compression geometry. The final strains were in the range of 6 to 23% depending on the strain-rate. The strain rates were determined by fitting the strain–time curves with a linear regression in the steady-state deformation range where the strain rate and the differential stresses remained almost constant. For low ($\sim 10^{-6} \text{ s}^{-1}$), intermediate ($\sim 5 \times 10^{-5} \text{ s}^{-1}$) and high ($\sim 10^{-4} \text{ s}^{-1}$) strain rates, uncertainties in these mean rates are 0.15%, 0.27% and 0.34% respectively.

2.4. *In situ* stress measurements

A total of 512 diffraction images were collected during deformation for the four runs. They were divided into 36 azimuthal angular regions at 10° interval. The data in these 10° intervals were integrated and converted into one dimensional spectra (intensity versus 2θ angle). Diffraction peak position and background were fitted for all the intervals in each diffraction patterns using Multifit and Polydefix softwares developed by Sebastian

Merkel (available online at <http://merkel.zoneo.net/Multifit/>). We obtained the azimuthal dependence of d-spacing, from which stress is calculated using the lattice strain model (Singh et al., 1998).

In axial compression the stress applied on the specimen can be expressed as:

$$\sigma_{ij} = \begin{vmatrix} \sigma_1 & 0 & 0 \\ 0 & \sigma_2 & 0 \\ 0 & 0 & \sigma_3 \end{vmatrix} = \begin{vmatrix} \sigma_P & 0 & 0 \\ 0 & \sigma_P & 0 \\ 0 & 0 & \sigma_P \end{vmatrix} + \begin{vmatrix} -\tau/3 & 0 & 0 \\ 0 & -\tau/3 & 0 \\ 0 & 0 & 2\tau/3 \end{vmatrix} \quad (1)$$

$$= \sigma_P + D_{ij}$$

where $\sigma_1 = \sigma_2$, σ_1 and σ_3 are radial and axial stress components respectively, $\tau = \sigma_3 - \sigma_1$ is the differential stress. σ_P is the hydrostatic or isotropic mean stress usually named “confining pressure” in deformation experiments and in this study and D_{ij} is the deviatoric stress tensor.

The lattice strain model (Singh et al., 1998) relates the lattice elastic strains to the applied stress via the elastic properties of the material.

$$d_{(hkl)}^m = d_{(hkl)}^p \left(1 + \frac{t_{(hkl)}}{3} (1 - 3\cos^2\psi) \frac{1}{2G_{hkl}} \right) \quad (2)$$

where $d_{(hkl)}^m$ is the measured d-spacing of the diffracting (hkl) plane, $d_{(hkl)}^p$ is the d-spacing of the diffracting (hkl) plane under hydrostatic stress, and $t_{(hkl)}$ is the differential stress, ψ is the angle between the diffracting plane normal and the deformation axis direction, related to the azimuth δ on the 2D detector by $\cos\psi = \cos\theta \cos(\delta - \delta_c)$ where θ is the diffraction angle and δ_c is the azimuth of the compression direction on the detector.

Hydrostatic lattice parameters $d_{(hkl)}^p$ gives the unit cell volume of each material under hydrostatic conditions used to calculate the hydrostatic mean stress (confining pressure) with the equation of state of the sample (Hilairet et al., 2006) and of gold

Table 1
Elastic constants obtained from our DFT calculations and used for $G(hkl)$ calculations (GPa).

(GPa)	M_0	M'
C_{11}	226	−1.7
C_{33}	76.7	14.3
C_{12}	79.2	−3.1
C_{13}	6.6	6.1
C_{44}	20.2	−1.2

Table 2

Experimental conditions and corresponding stresses and strain rates calculated for lizardite deformation experiments (see Section 2.2 Deformation experiments, Section 2.3 *In situ* strain measurements and Section 2.4 *In situ* stress measurements for details on uncertainty).

# run	Grain size (μm)	P (GPa)	T ($^{\circ}\text{K}$)	$\sigma_{(hkl)}$ (MPa)				$\dot{\epsilon}$ (10^{-5} s^{-1})	Total strain (%)
				001	002	111	112		
D1064	< 10	7.7	523	2020	1840	150	40	0.66	10.0
		8.1	523	2180	1970	160	80	9.65	19.2
		7.8	673	1770	1600	140	80	8.41	17.5
D1065	50–100	7.2	423	1590	1520	120	40	0.59	9.5
		7.7	423	1990	1860	180	40	11.94	25.7
		6.8	523	1870	1720	240	100	0.94	12.2
		6.8	523	2160	2200	190	110	15.70	22.0
D1130	< 10	3.3	523	810	800	170	70	1.06	13.2
		3.5	523	950	820	190	80	4.34	14.9
		2.5	673	560	320	160	110	0.83	12.5
		2.5	673	530	340	160	110	3.80	15.1
D1131	< 10	1.7	523	510	490	130	50	1.02	19.6
		1.5	523	300	330	120	70	3.43	14.9
		0.8	673	450	380	130	80	1.00	22.4

(Anderson et al., 1989). Confining pressure increased slightly during deformation cycles. Values reported in the Table 1 correspond to the average confining pressure on the sample during the steady-state deformation. Uncertainties are ± 0.25 GPa for confining pressure below 2 GPa, ± 0.5 GPa for pressure between 2 and 3 GPa and ± 0.8 GPa for pressure above 6 GPa. The shear moduli G_{hkl} in Eq. (2) are calculated under σ_P and the Reuss conditions using hexagonal crystallographic system and elastic constants obtained from our DFT calculations (Table 1; see next section). Temperature effects were calculated using the computed pressure variations of elastic constant and assuming a quasi-harmonic approximation with a thermal expansivity of $3.3 \times 10^{-5} \text{ K}^{-1}$ (Gregorkiewicz et al., 1996). A 500 $^{\circ}\text{C}$ variation results in 10% variation on the differential stresses whatever the confining pressure or the crystallographic planes considered.

For each experimental set of conditions (T , P , $\dot{\epsilon}$) we obtained differential stresses for 4 diffracting crystallographic planes. Differential stress values reported in Table 2 correspond to the average of stresses calculated for each crystallographic plane in steady-state deformation.

2.5. Computational

We performed first-principles calculations based on the Density Functional Theory (DFT) in the ABINIT implementation (Gonze et al., 2002; Gonze et al., 2005a; Gonze et al., 2009). We employed Density-Functional Perturbation Theory (DFPT) (Baroni et al., 1987, 2001; Gonze and Vigneron, 1989; Gonze and Lee, 1997; Gonze et al., 2005b) in the Perdew, Burke, Ernzerhof formulation (Perdew et al., 1996) of the Generalized-Gradient Approximation (GGA) to compute the elastic constants tensor. In this extension of DFPT (Hamann et al., 2005), the elastic tensor is computed analytically as the derivative of

the energy with respect to lattice strains and corrected for the atomic relaxations using the interatomic force constants tensors and the derivatives with respect to electric fields.

In a separate set of calculations we used the Planar Augmented Wavefunction (PAW) approach to compute the gamma-surfaces and to estimate the Critical Resolved Shear Stresses (CRSS). In the PAW method an all-electron representation of the electronic system is placed in correspondence with a pseudopotential-like treatment of the valence electrons (Blochl, 1994; Torrent et al., 2008). A set of spheres is defined around the atoms. Inside the spheres the density is described in the all-electron representation, outside using the pseudopotential-like treatment. Then, two grids are defined for the description of the wavefunctions: a radial finer grid inside the PAW sphere and a regular coarser mesh in the whole simulation cell. The correspondence of the two electronic treatments is ensured on the points common to the two grids.

We computed the gamma surfaces in two steps. First we fully relaxed the lizardite crystal structure at 1 and 3 GPa. Then we simulated the (001) dislocation plane by taking a slab formed of two constituent layers and displacing one layer with respect to the other in 0.1 steps (reduced coordinates) along both x and y directions. The two layers are separated by 10 Bohr (5.29166 Å) of vacuum by their translationally equivalent image along the [001] direction. At each lateral displacement we fix the external atomic layer on each side and allow the structural relaxation of all the other atoms only along the direction perpendicular to (001). We compare the energy of the resulting structure to the energy of the undisplaced stacking. The result is the energy variation on the dislocation slip plane. The CRSS are computed using the Peierls–Navarro method (Carrez and Cordier, 2010).

2.6. Preparation of recovered samples

High-pressure cells recovered from deformation experiments were embedded in epoxy, cut parallel to the compression axis and polished with alumina down to 1/20 μm . These sections were observed using an Environmental Scanning Electron Microscope XL30 FEI (Fig. 2b). From these half-cells, Transmission Electron Microscopy (TEM) thin sections were extracted parallel to the differential stress compression axis using a Focused Ion Beam on a ZEISS NVision 40 (Fig. 2c). All milling was performed with a 30 kV ion beam. Samples were coated with a 20 nm-thick carbon layer. Amorphisation of the sub-surface during FIB preparation was avoided by two-step deposition of W protective layers. First a 10–15 nm-thick W layer by electron-beam deposition, and second a 0.2 mm layer by ion-beam deposition on a surface of about $2.5 \times 25 \mu\text{m}^2$. A final carbon coating of 2 μm was added on the zone prepared for milling. Two excavations were made on top and bottom of the future TEM lamella location. TEM lamellae were separated from the bulk of the sample and lifted out when a thickness between 1 and 2 μm was reached. They were fixed by C or W deposition on a half copper grid on V-position as illustrated on figure. The TEM lamellae thickness was decreased to the desired value of 80–120 nm for TEM observations with decreasing ion beam current from 700 pA to 80 pA as the desired foil thickness was approached. The TEM lamellae were then cleaned of traces of Ga ion implantation at 2 kV–50 pA during 3–5 min on each side. These TEM thin sections were observed using a Jeol 200CX apparatus operating at 200 kV.

3. Results

3.1. Mechanical data

We obtained strains and stresses from X-Ray radiographs and diffraction patterns, respectively. Elastic constants obtained from

first-principles calculations based on Density-Functional Theory (DFT) allowed us to convert lattice strain into stresses (Table 1). Results are reported as stress–strain curves for 14 (P–T– $\dot{\epsilon}$) conditions on 4 different samples (Table 1). Lizardite samples were deformed up to 25% total strain.

In previous deformation experiments using X-ray diffraction, the dispersion of the differential stresses inferred from distortion of diffraction lines reaches 30% for olivine (Durham et al., 2009), antigorite (Hilairt et al., 2007) or quartz (Burnley and Zhang, 2008). Although the calculation of the average of the differential stresses recorded by crystallographic planes does not provide the real macroscopic stress state of the polycrystal (Burnley and Zhang, 2008; Merkel et al., 2009, 2012), it is a first-order approximation to the flow stress of the material. In lizardite, the difference between stresses inferred from {001} and (111) reflections is of a factor from 5 to 20, rendering calculating average stress values meaningless. This large rheological anisotropy is the combination of the specific mechanical properties of lizardite and the development of a strong Crystal Preferred Orientation during compression and deformation with preferential alignment of the basal {001} planes normal to the differential stress compression axis. In the experimental geometry, lattice strains on (111) d-spacing correspond to those crystals where basal planes are oblique to the compression, allowing glide on (001) (unlocked geometry). Thus inferred stresses on these planes are interpreted as yield stress for plastic flow of lizardite, in the range 50–200 MPa over the entire set of experimental conditions. In contrast, the stresses inferred from distortion of the {001} reflections correspond to the elastic response of crystals whose orientation precludes glide on (001) (locked geometry). They are much higher (500–2500 MPa) than those recorded by (111) planes, and increase strongly with increasing pressure (Figs. 3 and 4).

Easy gliding on lizardite basal plane was confirmed by first-principles calculations. The Critical Resolved Shear Stress (CRSS)

on (001) was obtained by calculating the energy needed to translate individual layers of lizardite with respect to each other. Results for translation in the basal planes (Fig. 5) indicate CRSS of less than 80 MPa and 120 MPa for pressures of 1 and 3 GPa, respectively. These low values are in quantitative agreement with the measured yield stress for plastic flow (Figs. 3 and 4), and account for the TEM observation of basal glide as the dominant deformation mechanism.

3.2. Microstructures

Samples recovered from high-pressure deformation experiments show plastic deformation features, and no evidence of brittle failure. Horizontal cracks visible on Fig. 2b were formed during cold decompression when the deformation was stopped. Transmission Electron Microscopy (TEM) observations were performed on Focused Ion Beam (FIB) thin sections (Fig. 2c) extracted along the compression direction. Lizardite crystals deformed by kinking (Fig. 1d), whatever the grain size of the starting material and the deformation conditions. Kink domain orientation indicates glide on (001) (Viti and Hirose, 2009), with kink boundaries at angles above 60° to (001) and high tilt angles (up to 50°) between domains. The amount of deformation due to kinks at the microscopic scale is similar to the total macroscopic sample strain (Fig. 2d). This indicates that plastic flow was homogeneous from millimeter to micrometer scale in the experiments.

4. Discussion

4.1. Role of phyllosilicate structure on mechanical behaviour

The structure of lizardite explains its peculiar mechanical response with respect to antigorite (Hilairt et al., 2007; Chernak and Hirth,

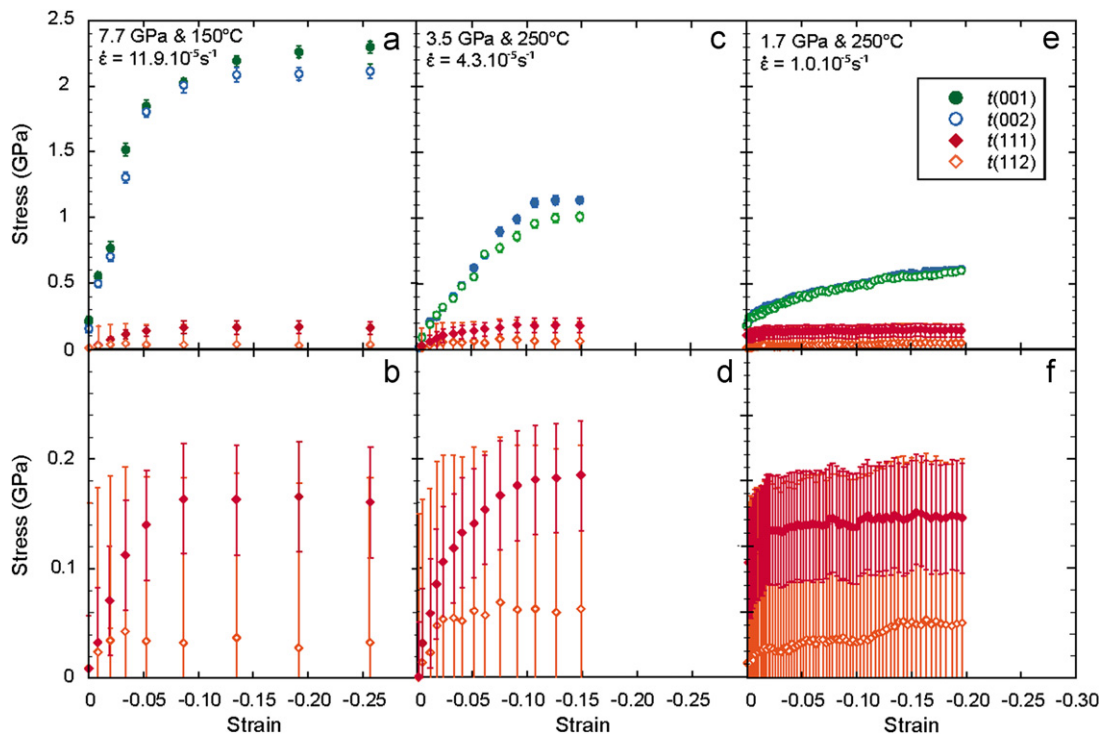


Fig. 3. Stress–strain curves obtained for lizardite (hkl) planes at different experimental conditions. (a, c and e) Differential stresses recorded for both {001} and (111) lizardite planes. (b, d and f) Blow up of differential stresses recorded by (111) planes for the same experimental conditions as a, c and e respectively. Stresses measured on {001} planes correspond to the elastic response of the material. They increase strongly with increasing pressure. Differential stresses measured on (111) planes are representative of the plastic flow of lizardite. We do not detect variations of (111) stresses with pressure, temperature and strain rate within experimental errors.

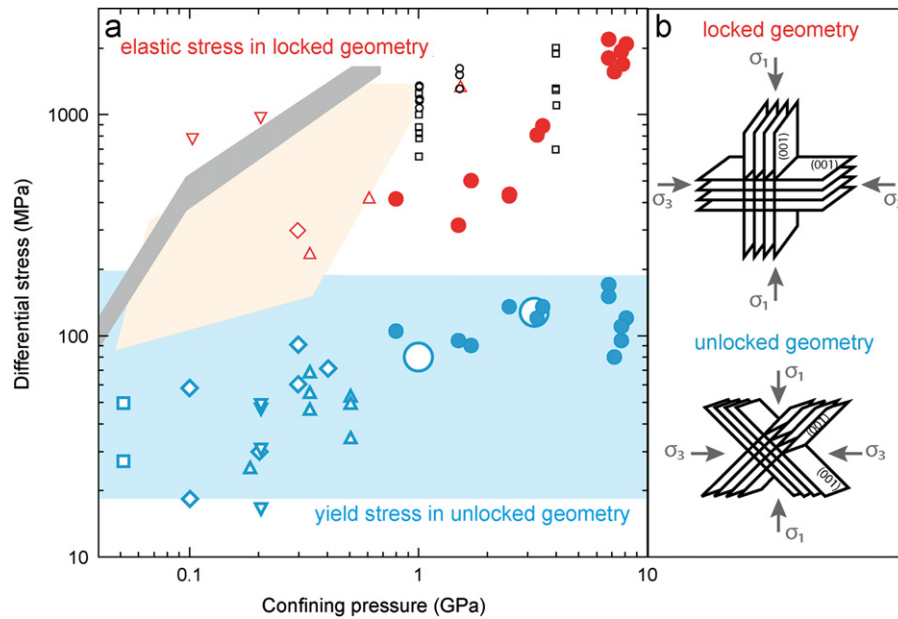


Fig. 4. Experimental stress of deforming serpentine and phyllosilicates. (a) Yield stresses of lizardite (blue circles, this work) and micas (blue upward triangles for biotite (Kronenberg et al., 1990); blue downward triangles and diamonds for muscovite single crystals, and polycrystal respectively; (Mares and Kronenberg, 1993; Misra and Burg, 2012)). Stresses for unlocked geometry are similar to DFT slip energies (blue empty circles) and fall in the range allowing the onset of plate tectonics in geodynamical models (blue area). Talc values (squares (Escartin et al., 2008)) also fall in this area. Red symbols correspond to elastic stresses in a locked geometry. Orange area covers the stresses measured on serpentine and mica rock samples (Raleigh and Paterson, 1965; Shea and Kronenberg, 1992). Data for foliated muscovite aggregates deformed in torsion experiments (Misra and Burg, 2012) fall close to those of unlocked single-crystals geometry. Yield stresses for the antigorite serpentine variety are shown for comparison (black circles and squares, ((Chernak and Hirth, 2010; Hilairet et al., 2007), respectively). Byerlee's friction law is shown as a thick grey line. (b) The stresses measured on vertical and horizontal (001) planes correspond to locked geometries where glide is inhibited because of negligible Schmid factors (no shear stress) on the glide plane. Stresses measured on (111) correspond to unlocked geometries where the Schmid factor is high on the {001} planes. (For interpretation of the references to colour in this figure legend, the reader is referred to the web version of this article.)

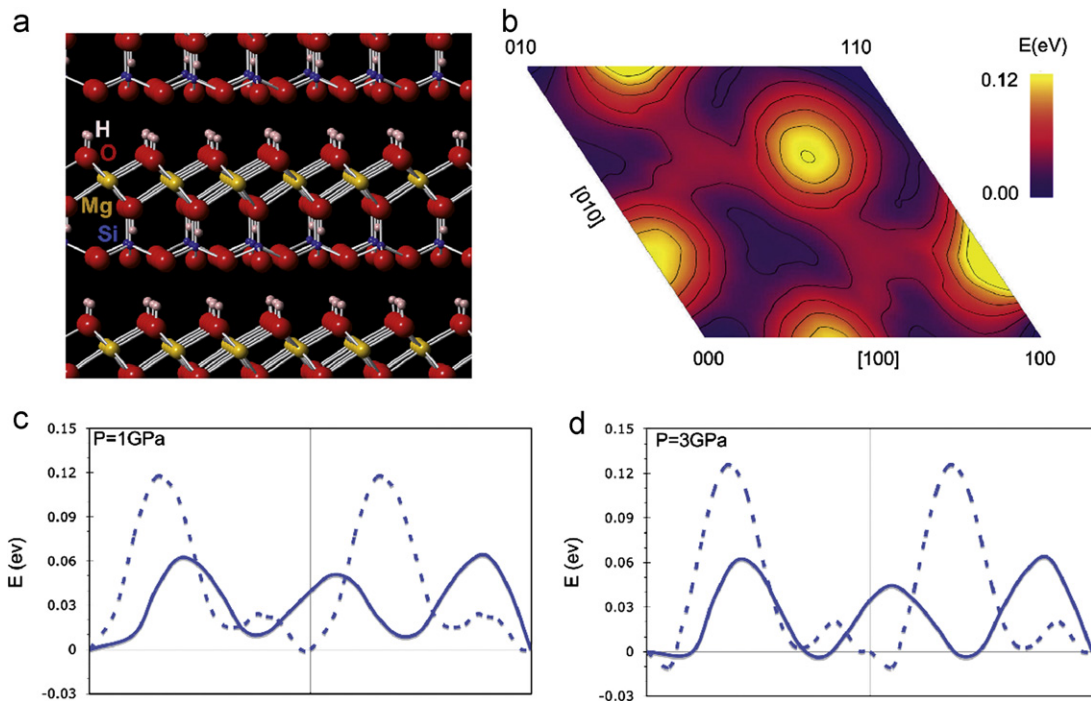


Fig. 5. Computed structure and critical resolved shear stress in lizardite. (a) Crystal structure at 1 GPa. (b) Gamma-surface on the (001) dislocation plane at 1 GPa in lizardite is obtained by displacing two layers along the (001) plane. Atoms are allowed to accommodate the displacement only in the perpendicular direction. The energy difference between the perfect crystal and sheared structures is mapped for various displacements in the basal plane. (c) and (d) Energy curves calculated along [100] (dashed curves) and $\langle 210 \rangle$ (full curves, easiest glide direction) directions at 1 and 3 GPa, respectively.

2010) and dry olivine (Mei et al., 2010) at low temperatures of subduction zones. Lizardite is an archetypal structure to major rock-forming hydrous phyllosilicates with a planar structure, such as

chlorite and many clay minerals. Sheet structural units are bonded by weak interactions between OH groups and silicate layers, allowing easy (001) glide where no strong silicate bonds are broken (Fig. 5a).

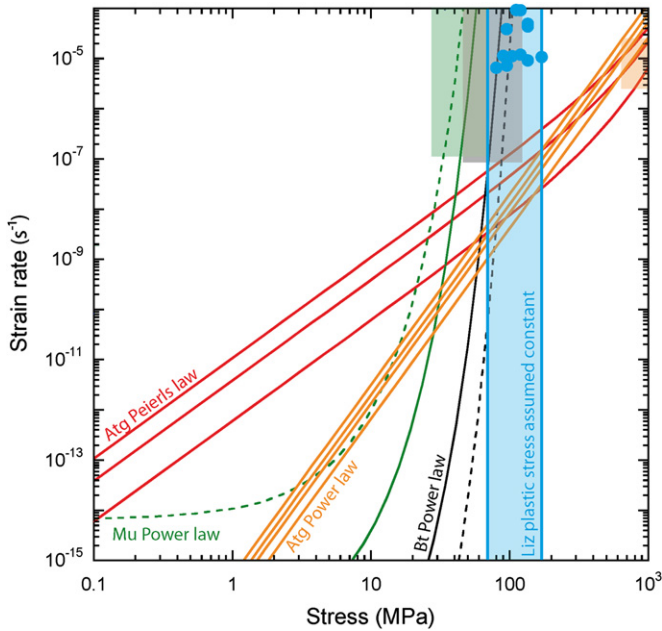


Fig. 6. Rheological behaviour of phyllosilicates. Blue circles represent the plastic flow of lizardite (Liz) recorded by (111) planes in this study. Coloured areas represent experimental data set in green for muscovite (Mares and Kronenberg, 1993), in grey for biotite (Kronenberg et al., 1990) and in orange for antigorite (Hilaret et al., 2007) from which rheological flow laws were extrapolated. Extrapolation of antigorite (Atg) flow laws using a Peierls law (red curves) calculated for 200 °C, 400 °C and 600 °C from bottom to top, and a power law (orange curves) calculated for 400 °C and 600 °C and for two pressures 1 GPa (two upper lines) and 3 GPa (two bottom lines). Flow laws for micas are represented in green for muscovite (Mu) and in black for biotite (Bt) for room T . A temperature increase from room T to 600 °C leads to a decrease by a factor 2 or 3 of the flow stresses for micas. Dashed and solid lines are used to distinguish the easiest slip directions from harder slip directions, respectively. Mica behaviour is close to that of a plastic solid as assumed here for lizardite. (For interpretation of the references to colour in this figure legend, the reader is referred to the web version of this article.)

It is similar to that observed in mica phyllosilicates (Kronenberg et al., 1990; Mares and Kronenberg, 1993) where glide along the basal planes breaks weak K–O bonds between silicate layers. In antigorite, the corrugation of the stacking sequence makes plastic flow more difficult (Fig. 4). Low yield stresses were maintained over large strains during simple shearing of muscovite aggregates (Misra and Burg, 2012). Thus foliated lizardite serpentinites will evolve towards and maintain low yield stress during progressive deformation when the (001) planes align along the shear directions.

The yield strength of lizardite lies within the critical range for initiating subduction and plate tectonics at strain rates as large as 10^{-4} s^{-1} (Fig. 4 and Fig. 6). We cannot observe a systematic dependence of yield strengths on strain rate, grain size, pressure or temperature within experimental uncertainties. Deformation experiments on single-crystal micas show measurable small dependence of stress on temperature and strain rate (Kronenberg et al., 1990; Mares and Kronenberg, 1993), beyond the accuracy of the present study. Such high-precision experiments could not be reproduced on lizardite because no large single-crystal can be found. Given their structural similarities, results on micas can be used to assess the temperature and strain-rate dependence of yield stress of lizardite at geological strain rates. Yield stress of lizardite should decrease with increasing temperature and decreasing strain rate.

4.2. Rheological laws for natural serpentinites

Hydrothermal activity and serpentinitisation will reduce significantly the yield stress of mafic and ultramafic rocks down to

20–30 km depths in cold geotherms (Hirauchi et al., 2010) from values up to 2–3 GPa for dry rocks down to a few tens of MPa for serpentinites. The stable serpentine variety depends on metamorphic grade. Lizardite is a low temperature serpentine that transforms to antigorite at 300–350 °C (Evans, 2004). Low-temperature hydrothermal alteration in the first tens of kilometers of the primitive lithosphere is likely to have produced lizardite and the weak zones required for the initiation of plate tectonics. Serpentine is commonly found in the early Archean Isua belt for which ophiolitic affinity and hydrothermal activity have been proposed (Furnes et al., 2007). Antigorite is the common variety of serpentine in these setting, but petrological observations suggest it has formed during amphibolite-facies metamorphism from former low-temperature lizardite (Dymek et al., 1988).

Flow laws for phyllosilicates were extrapolated to stresses in the critical range 20–200 MPa (Fig. 6). Two flow laws were used for antigorite, a power law (Eq. (3)) (Hilaret et al., 2007) and a Peierls law (Eq. (4)) (Katayama and Karato, 2008):

$$\dot{\epsilon} = 4.10^{-38} \sigma^{3.8} \exp\left(\frac{8.9 \text{ kJ mol}^{-1} + P \times 3.2 \text{ cm}^3 \text{ mol}^{-1}}{RT}\right) \quad (3)$$

$$\dot{\epsilon} = 10^{-9.4} \times \sigma^2 \exp\left(\frac{-27 \text{ kJ mol}^{-1}}{RT}\right) \left(1 - \frac{\sigma}{\tau}\right) \quad (4)$$

where $\dot{\epsilon}$ is the strain rate, σ is the differential stress, τ is the Peierls stress equal to 2.7 GPa, P is the hydrostatic pressure, R is the gas constant and T is the temperature.

Flow laws for muscovite (Mares and Kronenberg, 1993) (Eq. (5)) and biotite (Kronenberg et al., 1990) (Eq. (6)) are also reported in Fig. 6 corresponding to:

$$\dot{\epsilon} = C \exp(0.5 \text{ MPa}^{-1} \sigma) \exp\left(\frac{-47 \text{ kJ mol}^{-1}}{RT}\right) \quad (5)$$

with $C = 4 \times 10^{-9}$ and $C = 1 \times 10^{-6}$

$$\dot{\epsilon} = C \exp(0.41 \text{ MPa}^{-1} \sigma) \exp\left(\frac{-82 \text{ kJ mol}^{-1}}{RT}\right) \quad (6)$$

with $C = 4.6 \times 10^{-6}$ and $C = 4.3 \times 10^{-9}$ where $\dot{\epsilon}$ is the strain rate, C is a constant depending on slip directions.

For lizardite, our data on flow have a lower resolution than external measurements performed on micas. Thus we cannot assess the temperature and stress dependence of strain rates and derive directly a flow law. We assume that given the similarities of stresses in lizardite and micas, the flow laws should be similar. Flow laws for single-crystal micas indicate very small decrease of flow stress with decreasing strain rates and increasing temperature. Thus, the present experimental results are upper bounds to the yield stress of single-crystal lizardite in both experimental and natural conditions, assuming a perfectly plastic behaviour (Fig. 6).

Recent results on deformation experiments on muscovite aggregate (Misra and Burg, 2012) allow to predict flow strength of lizardite in simple shear deformation geometry considered in natural contexts. Macroscopic flow stress (20–90 MPa) of muscovite polycrystal in torsion geometry corresponding to the unlocked geometry increases with increasing pressure and decreasing temperature at constant strain rate ($3 \times 10^{-4} \text{ s}^{-1}$). In uniaxial compression corresponding to the locked geometry where basal planes are perpendicular to deformation compression axis, macroscopic stress is much higher (300 MPa) for the same experimental conditions. These results are in good agreement with our observations. In simple shear geometry, corresponding to subduction zones and deep portion of active fault, the flow

strength of lizardite will be comparable to that inferred from (111) diffraction lines (Fig. 6).

4.3. Role of weak phyllosilicates in plate tectonics.

Extrapolation of flow laws for antigorite at stresses of 20–200 MPa yields strain rates in the range 10^{-6} – 10^{-9} s⁻¹ for a fit to Peierls law and 10^{-7} – 10^{-11} s⁻¹ for power law. Such strain rates are well above typical convection rates of 10^{-13} – 10^{-15} s⁻¹, and correspond to rates in localised shear zones or faults. A close link between hydrothermal alteration and weakening of crustal rocks was demonstrated (Wintsch et al., 1995) based on rheological studies of micas (Kronenberg et al., 1990; Mares and Kronenberg, 1993) for pressures up to 0.5 GPa, which correspond to approximately 15 km depth. The present dataset on lizardite extends these results to mafic and ultramafic systems and to pressures up to 7 GPa corresponding to equivalent depths of more than 200 km.

Mechanically weak lizardite is an archetypal structure to major rock-forming hydrous phyllosilicates, such as chlorite and talc that form from hydrothermal alteration of basic to ultrabasic rocks. Thus, chlorite is likely to have a low yield stress because it has similar interlayer bonds to lizardite. Chlorite is also a common mineral in many ophiolites, starting from the Eo-Archean the Isua belt (Komiya et al., 1999). Chlorite has a higher maximum-temperature of stability (about 750 °C) than lizardite and antigorite, and may provide an additional weak material for subduction to greater depths than serpentines. Talc structure also favours low yield strength, and accounts for regional rheological heterogeneities even as a minor rock component (Moore and Rymer, 2007).

Thus there exists a continuum of stable phyllosilicates with low yield stresses for metamorphic grades ranging from about 150 °C (lizardite then antigorite) to 750 °C (chlorite) up to pressures of 7 GPa. It allows the generation and the maintenance of stable weak hydrated zones throughout the crust and the lithospheric mantle to depths of 30 km for a hot geotherm, and down to about 150 km for a cold subduction geotherm. These depths encompass the range over which the dry lithosphere is too stiff to allow strain localization leading to plate generation and subduction.

Such a suite of phyllosilicates existed as early as 3.8 Ga ago in the Isua belt supporting the petrological and geochemical arguments in favor of an early onset of plate-like tectonics on Earth (Komiya et al., 1999; Polat et al., 2002; Harrison et al., 2005). Serpentines, including lizardite, are found in rock fragments exhumed by serpentine mud volcanoes above the active oceanic Izu-Bonin subduction zone (Fryer and Mottl, 1992). In this oceanic subduction zone, the aseismic region corresponds to shallow depths (15–20 km) where large amount of fluids are released by the subducting slab leading to extensive serpentinisation of the Izu-Bonin mantle wedge.

The low seismicity and the absence of large earthquakes along the shallow part of the plate boundary in this region is associated with serpentinisation (Kamimura et al., 2002). The low yield strength of lizardite determined here for plastic flow deformation demonstrates that phyllosilicates could be responsible for aseismic sliding and lead to weak slab-mantle coupling.

Present-day oceanic subduction zones such as the Izu-Bonin segment may be viewed as analogues of early subduction zones. The presence of water and development of weak hydrated zones may have promoted the initiation of plate tectonics by mechanisms that are not available on other telluric planets (Regenauer-Lieb et al., 2001; Bercovici, 2003). Areas like the Tonga-Kermadec and western Aleutian segments are potential targets for further systematic investigation of links between serpentinization and mechanical weakening.

Other potential sites for initiation of subduction are transform faults (Bercovici, 2003; Hall et al., 2003), which are active sites of hydrothermal activity and serpentinisation.

Acknowledgments

We thank S. Merkel, P. Cordier and I. Katayama for insightful discussions and A. Kronenberg and an anonymous reviewer for their constructive comments, which greatly improved the manuscript. This study was supported by ANR project SUBDEF grant no. ANR-08-BLAN-0192 to BR. Deformation experiments were performed at GeoSoilEnviroCARS (Sector 13), Advanced Photon Source (APS), Argonne National Laboratory. GeoSoilEnviroCARS is supported by the (National Science Foundation - Earth Sciences EAR-1128799) and Department of Energy - Geosciences (DE-FG02-94ER14466). Use of the Advanced Photon Source was supported by the US Department of Energy, Office of Science, Office of Basic Energy Sciences, under Contract no. DE-AC02-06CH11357. YW acknowledges financial support from the National Science Foundation (EAR-0968456). FIB thin sections and TEM images were obtained at CLYM (CNRS, FED 4092) and MATEIS Laboratory at INSA in Lyon, France, respectively.

References

- Anderson, O.L., Isaak, D.G., Yamamoto, S., 1989. Anharmonicity and the equation of state for gold. *J. Appl. Phys.* 65, 1534–1543.
- Baroni, S., Giannozzi, P., Testa, A., 1987. Green-function approach to linear response in solids. *Phys. Rev. Lett.* 58, 1861–1864.
- Baroni, S., de Gironcoli, S., Dal Corso, A., Giannozzi, P., 2001. Phonons and related crystal properties from density-functional perturbation theory. *Rev. Mod. Phys.* 73, 515–562.
- Bercovici, D., 2003. The generation of plate tectonics from mantle convection. *Earth Planet Sci. Lett.* 205, 107–121.
- Bercovici, D., Ricard, Y., 2012. Mechanisms for the generation of plate tectonics by two-phase grain-damage and pinning. *Phys. Earth Planet Interiors.*
- Blichert-Toft, J., Albarede, F., 2008. Hafnium isotopes in Jack Hills zircons and the formation of the Hadean crust. *Earth Planet Sci. Lett.* 265, 686–702.
- Bloch, P.E., 1994. Projector augmented-wave method. *Phys. Rev. B* 50, 17953–17979.
- Burnley, P.C., Zhang, D., 2008. Interpreting *in situ* x-ray diffraction data from high pressure deformation experiments using elastic-plastic self-consistent models: an example using quartz. *J. Phys.: Condens. Matter* 20, 285201.
- Byerlee, J., 1978. Friction of rocks. *Pure Appl. Geophys.* 116, 615–626.
- Carrez, P., Cordier, P., 2010. Modeling dislocations and plasticity of deep earth materials. *Rev. Mineral Geochem.* 71, 225–251.
- Chernak, L.J., Hirth, G., 2010. Deformation of antigorite serpentine at high temperature and pressure. *Earth Planet Sci. Lett.* 296, 23–33.
- Durham, W.B., Mei, S., Kohlstedt, D.L., Wang, L., Dixon, N. a., 2009. New measurements of activation volume in olivine under anhydrous conditions. *Phys. Earth Planet Interiors* 172, 67–73.
- Dymek, R.F., Boak, J.L., Brothers, S.C., 1988. Titanian chondrodite-bearing and titanian clinohumite-bearing metadunite from the 3800 Ma Isua supracrustal belt, West Greenland—chemistry, petrology, and origin. *Amer. Mineral* 73, 547–558.
- Escartin, J., Andreani, M., Hirth, G., Evans, B., 2008. Relationships between the microstructural evolution and the rheology of talc at elevated pressures and temperatures. *Earth Planet Sci. Lett.* 268, 463–475.
- Escartin, J., Hirth, G., Evans, B., 1997a. Effects of serpentinization on the lithospheric strength and the style of normal faulting at slow-spreading ridges. *Earth Planet Sci. Lett.* 151, 181–189.
- Escartin, J., Hirth, G., Evans, B., 1997b. Effects of serpentinization on the lithospheric strength and the style of normal faulting at slow-spreading ridges. *Earth Planet Sci. Lett.* 151, 181–189.
- Escartin, J., 2003. Constraints on deformation conditions and the origin of oceanic detachments: The Mid-Atlantic Ridge core complex at 15°45'N. *Geochem. Geophys. Geosyst.*, 4.
- Evans, B.W., 2004. The serpentine multystem revisited: Chrysotile is metastable. *Int. Geol. Rev.* 46, 479–506.
- Fryer, P., Mottl, M.J., 1992. Lithology, mineralogy, and origin of serpentine muds recovered from conical and torishima forearc seamounts: results of leg 125 drilling 1 Conical Seamount. In: Fryer, P., Pearce, J.A., Stokking, L.B. (Eds.), *Proceedings of the Ocean Drilling Program, Scientific Results*. pp. 343–362.
- Furnes, H., de Wit, M., Staudigel, H., Rosing, M., Muehlenbachs, K., 2007. A vestige of Earth's oldest ophiolite. *Science* 315, 1704–1707.
- Gonze, X., Amadon, B., Anglade, P.M., Beuken, J.M., Bottin, F., Boulanger, P., Bruneval, F., Caliste, D., Caracas, R., Cote, M., Deutsch, T., Genovese, L., Ghosez, P., Giantomassi, M., Goedecker, S., Hamann, D.R., Hermet, P.,

- Jollet, F., Jomard, G., Leroux, S., Mancini, M., Mazevet, S., Oliveira, M.J.T., Onida, G., Pouillon, Y., Rangel, T., Rignanesse, G.M., Sangalli, D., Shaltaf, R., Torrent, M., Verstraete, M.J., Zerah, G., Zwanziger, J.W., 2009. ABINIT: First-principles approach to material and nanosystem properties. *Comput. Phys. Commun.* 180, 2582–2615.
- Gonze, X., Beuken, J.M., Caracas, R., Detraux, F., Fuchs, M., Rignanesse, G.M., Sindic, L., Verstraete, M., Zerah, G., Jollet, F., Torrent, M., Roy, A., Mikami, M., Ghosez, P., Raty, J.Y., Allan, D.C., 2002. First-principles computation of material properties: the ABINIT software project. *Comput. Mater. Sci.* 25, 478–492.
- Gonze, X., Lee, C., 1997. Dynamical matrices, born effective charges, dielectric permittivity tensors, and interatomic force constants from density-functional perturbation theory. *Phys. Rev. B* 55, 10355–10368.
- Gonze, X., Rignanesse, G.M., Caracas, R., 2005a. First-principle studies of the lattice dynamics of crystals, and related properties. *Z. Kristallogr.* 220, 458–472.
- Gonze, X., Rignanesse, G.M., Verstraete, M., Beuken, J.M., Pouillon, Y., Caracas, R., Jollet, F., Torrent, M., Zerah, G., Mikami, M., Ghosez, P., Veithen, M., Raty, J.Y., Olevano, V., Bruneval, F., Reining, L., Godby, R., Onida, G., Hamann, D.R., Allan, D.C., 2005b. A brief introduction to the ABINIT software package. *Z. Kristallogr.* 220, 558–562.
- Gonze, X., Vigneron, J.P., 1989. Density-functional approach to nonlinear-response coefficients of solids. *Phys. Rev. B* 39, 13120–13128.
- Gregorkiewicz, M., Lebeck, B., Mellini, M., Viti, C., 1996. Hydrogen positions and thermal expansion in lizardite-1T from Elba: A low-temperature study using Rietveld refinement of neutron diffraction data. *Amer. Mineral* 81, 1111–1116.
- Hall, C.E., Gurnis, M., Sdrolias, M., Lavier, L.L., Müller, R.D., 2003. Catastrophic initiation of subduction following forced convergence across fracture zones. *Earth Planet Sci. Lett.* 212, 15–30.
- Hamann, D.R., Wu, X.F., Rabe, K.M., Vanderbilt, D., 2005. Metric tensor formulation of strain in density-functional perturbation theory. *Phys. Rev. B* 71.
- Harrison, T.M., Blichert-Toft, J., Muller, W., Albarede, F., Holden, P., Mojzsis, S.J., 2005. Heterogeneous Hadean hafnium: Evidence of continental crust at 4.4 to 4.5 Ga. *Science* 310, 1947–1950.
- Van Heck, H.J., Tackley, P.J., 2008. Planforms of self-consistently generated plates in 3D spherical geometry. *Geophys. Res. Lett.*, 35.
- Hilairt, N., Daniel, I., Reynard, B., 2006. P-V equations of state and the relative stabilities of serpentine varieties. *Phys. Chem. Miner.* 33, 629–637.
- Hilairt, N., Reynard, B., Wang, Y.B., Daniel, I., Merkel, S., Nishiyama, N., Petitgirard, S., 2007. High-pressure creep of serpentine, interseismic deformation, and initiation of subduction. *Science* 318, 1910–1913.
- Hirauchi, K., Katayama, I., Uehara, S., Miyahara, M., Takai, Y., 2010. Inhibition of subduction thrust earthquakes by low-temperature plastic flow in serpentine. *Earth Planet Sci. Lett.* 295, 349–357.
- Kamimura, A., Kasahara, J., Shinohara, M., Hino, R., Shiobara, H., Fujie, G., Kanazawa, T., 2002. Crustal structure study at the Izu-Bonin subduction zone around 31 degrees N: implications of serpentinized materials along the subduction plate boundary. *Phys. Earth Planet Interiors* 132, 105–129.
- Katayama, I., Karato, S.I., 2008. Low-temperature, high-stress deformation of olivine under water-saturated conditions. *Phys. Earth Planet Interiors* 168, 125–133.
- Komiya, T., Maruyama, S., Masuda, T., Nohda, S., Hayashi, M., Okamoto, K., 1999. Plate tectonics at 3.8–3.7 Ga: Field evidence from the Isua Accretionary Complex, southern West Greenland. *J. Geol.* 107, 515–554.
- Kronenberg, A.K., Kirby, S.H., Pinkston, J., 1990. Basal slip and mechanical anisotropy of biotite. *J. Geophys. Res.-Sol. Earth Planets* 95, 19257–19278.
- Maekawa, H., Shozul, M., Ishii, T., Fryer, P., Pearce, J.A., 1993. Blueschist metamorphism in an active subduction zone. *Nature* 364, 520–523.
- Mares, V.M., Kronenberg, A.K., 1993. Experimental deformation of muscovite. *J. Struct. Geol.* 15, 1061–1075.
- Mei, S., Suzuki, A.M., Kohlstedt, D.L., Dixon, N.A., Durham, W.B., 2010. Experimental constraints on the strength of the lithospheric mantle. *J. Geophys. Res.-Solid Earth*, 115.
- Mellini, M., Viti, C., 1994. Crystal-structure of lizardite-1t from Elba, Italy. *Amer. Mineral* 79, 1194–1198.
- Merkel, S., Gruson, M., Wang, Y., Nishiyama, N., Tomé, C.N., 2012. Texture and elastic strains in hcp-iron plastically deformed up to 17.5 GPa and 600 K: experiment and model. *Model Simul. Mater. Sci. Eng.* 20, 024005.
- Merkel, S., Tomé, C., Wenk, H.-R., 2009. Modeling analysis of the influence of plasticity on high pressure deformation of hcp-Co. *Phys. Rev. B* 79, 1–13.
- Misra, S., Burg, J.-P., 2012. Mechanics of kink-bands during torsion deformation of muscovite aggregate. *Tectonophysics* 548–549, 22–33.
- Mojzsis, S.J., Harrison, T.M., Pidgeon, R.T., 2001. Oxygen-isotope evidence from ancient zircons for liquid water at the Earth's surface 4300 Myr ago. *Nature* 409, 178–181.
- Moore, D.E., Lockner, D.A., Shengli, M., R., S., Byerlee, J.D., 1997. Strengths of serpentinites gouges at elevated temperatures. *J. Geophys. Res.* 102, 14787–14801.
- Moore, D.E., Rymer, M.J., 2007. Talc-bearing serpentinite and the creeping section of the San Andreas fault. *Nature* 448, 795–797.
- Murrell, S.A.F., Ismail, I.A.H., 1976. The effect of decomposition of hydrous minerals on the mechanical properties of rocks at high pressures and temperatures. *Tectonophysics* 31, 207–258.
- Mével, C., 2003. Serpentinization of abyssal peridotites at mid-ocean ridges. *C R Geosci.* 335, 825–852.
- Perdew, J.P., Burke, K., Ernzerhof, M., 1996. Generalized gradient approximation made simple. *Phys. Rev. Lett.* 77, 3865–3868.
- Polat, A., Hofmann, A.W., Rosing, M.T., 2002. Boninite-like volcanic rocks in the 3.7–3.8 Ga Isua greenstone belt, West Greenland: geochemical evidence for intra-oceanic subduction zone processes in the early Earth. *Chem. Geol.* 184, 231–254.
- Raleigh, C.B., Paterson, M.S., 1965a. Experimental deformation of serpentinite and its tectonic implications. *J. Geophys. Res.* 70, 3965.
- Raleigh, C.B., Paterson, M.S., 1965b. Experimental deformation of serpentinite and its tectonic implications. *J. Geophys. Res.* 70, 3965.
- Regenauer-Lieb, K., Yuen, D.A., Branlund, J., 2001. The initiation of subduction: Criticality by addition of water? *Science* 294, 578–580.
- Reinen, L.A., Weeks, J.D., Tullis, T.E., 1991. The frictional behavior of serpentinite: implications for aseismic creep on shallow crustal faults. *Geophys. Res. Lett.* 18, 1921–1924.
- Reinen, L.A., Weeks, J.D., Tullis, T.E., 1994. The frictional behavior of lizardite and antigorite serpentinites: experiments, constitutive models, and implications for natural faults. *Pure Appl. Geophys.* 143, 317–358.
- Shea, W.T., Kronenberg, A.K., 1992. Rheology and deformation mechanisms of an isotropic mica schist. *J. Geophys. Res.-Solid Earth* 97, 15201–15237.
- Singh, A.K., Balasingh, C., Mao, H.K., Hemley, R.J., Shu, J.F., 1998. Analysis of lattice strains measured under nonhydrostatic pressure. *J. Appl. Phys.* 83, 7567–7575.
- Solomatov, V.S., 2004. Initiation of subduction by small-scale convection. *J. Geophys. Res.-Solid Earth*, 109.
- Torrent, M., Jollet, F., Bottin, F., Zerah, G., Gonze, X., 2008. Implementation of the projector augmented-wave method in the ABINIT code: Application to the study of iron under pressure. *Comput. Mater. Sci.* 42, 337–351.
- Viti, C., Hirose, T., 2009. Dehydration reactions and micro/nanostructures in experimentally-deformed serpentinites. *Contrib. Mineral Petrol* 157, 327–338.
- Wang, Y.B., Durham, W.B., Getting, I.C., Weidner, D.J., 2003. The deformation-DIA: A new apparatus for high temperature triaxial deformation to pressures up to 15 GPa. *Rev. Sci. Instr.* 74, 3002–3011.
- Wang, Y.B., Rivers, M., Sutton, S., Nishiyama, N., Uchida, T., Sanehira, T., 2009. The large-volume high-pressure facility at GSECARS: A “Swiss-army-knife” approach to synchrotron-based experimental studies. *Phys. Earth Planet Interiors* 174, 270–281.
- Wintsch, R.P., Christoffersen, R., Kronenberg, A.K., 1995. Fluid-rock reaction weakening of fault zones. *J. Geophys. Res.-Solid Earth* 100, 13021–13032.